Journal of Power Sources 241 (2013) 266–273

Contents lists available at SciVerse ScienceDirect

Journal of Power Sources

journal homepage: www.elsevier.com/locate/jpowsour

Impedance-based study of capacitive porous carbon electrodes with hierarchical and bimodal porosity

Matthew E. Suss [a,b], Theodore F. Baumann [b], Marcus A. Worsley [b], Klint A. Rose [b], Thomas F. Jaramillo [c], Michael Stadermann [b,*], Juan G. Santiago [a,*]

[a] Department of Mechanical Engineering, 440 Escondido Mall, Stanford University, Stanford, CA 94305, USA
[b] Lawrence Livermore National Laboratory, 7000 East Avenue, Livermore, CA 94550, USA
[c] Department of Chemical Engineering, 381 North-South Mall, Stanford University, Stanford, CA 94305, USA

HIGHLIGHTS

- Novel framework for characterizing hierarchical and bimodal supercapacitor electrodes.
- First detailed characterization of hierarchical carbon aerogel monolith electrode set.
- Novel measurements and analysis of an HCAM electrode with sub-nanometer sized pores.

ARTICLE INFO

Article history:
Received 8 February 2013
Received in revised form
28 March 2013
Accepted 30 March 2013
Available online 16 April 2013

Keywords:
Energy storage
Carbon aerogel
Supercapacitor
Capacitive deionization
Electrochemical impedance spectroscopy
Hierarchical carbon

ABSTRACT

Porous electrode capacitors are used extensively in systems which store energy, harvest mixing energy, or desalinate water. These electrodes can possess a hierarchical pore structure with larger macroscale pores allowing for facile ion and fluid transport, and smaller, nanometer-scale pores enabling significant ion storage. We here present a combined theoretical (linear circuit model) and experimental (electrochemical impedance spectroscopy) study of porous carbon electrode capacitors which integrate nanoscale pores into a micron-scale porous network. Our experiments are performed on a set of custom-fabricated hierarchical carbon aerogel electrodes with varying pore structure, including electrodes with sub-nanometer (sub-nm) pores. Our combined theory and experimental approach allows us to demonstrate the utility of our model, perform detailed characterizations of our electrodes, study the effects of pore structure variations on impedance, and propose hierarchical electrode design and characterization guidelines. Further, we demonstrate that our approach is promising toward the detailed study of ion storage mechanisms in sub-nm pores.

© 2013 Elsevier B.V. All rights reserved.

1. Introduction

Porous carbon electrodes are extensively used as capacitors in many applications, including energy storage, energy harvesting, and water desalination [1–3]. In these systems, a pair of porous electrodes are filled with electrolyte and electrically charged. The resulting electric field causes ions in the liquid phase to transport into electric double layers (EDLs) on electrode surfaces. In electric double layer capacitors used for energy storage, ions are first stored in the EDLs, and subsequently the electrode pair is discharged through a load to deliver power on demand [3,4]. In energy harvesting applications, charged electrode pairs harvest the mixing energy of sea and river water through mechanisms such as EDL expansion/contraction or by leveraging the Donnan potential [2,5,6]. In desalination applications, charging the electrode pair removes significant amounts of salt ions from a liquid electrolyte (such as brackish water), and energy can be recovered when the ions are released into a brine stream [1,7–11].

In many porous electrode capacitor systems, the electrode pore structure consists largely of nanoscale pores in order to maximize ion storage capacity [1,11–13]. However, such a pore structure can limit charge and discharge kinetics by impeding ion transport [14]. High impedance to ion transport within the pore structure slows the temporal response, and so reduces device power density or increases time required for desalination. To prevent such transport limitations, several studies have proposed and analyzed electrode materials with

* Corresponding authors.
E-mail addresses: stadermann2@llnl.gov (M. Stadermann), juan.santiago@stanford.edu (J.G. Santiago).

0378-7753/$ – see front matter © 2013 Elsevier B.V. All rights reserved.
http://dx.doi.org/10.1016/j.jpowsour.2013.03.178

a hierarchical pore structure [7,15–19]. These electrodes typically contain a continuous, larger diameter pore network for low-resistance ion transport (typically macro- or mesoscale pores). These larger pores connect to smaller diameter pores that provide high specific surface areas used for ion storage (typically micro- or mesoscale pores). In addition to potentially improving ion transport, hierarchical electrodes lower the resistance to fluid flow through the electrode. Low impedance to fluid flow is essential for desalination devices with "flow-through" architecture wherein feed stream is transported primarily through the electrode itself [7].

Electrochemical impedance spectroscopy (EIS) measurements of porous electrode impedance have proven to be a powerful tool in electrode design and characterization, and have been used extensively [4]. However, circuit models commonly used to interpret porous electrode impedance are not appropriate for porous electrodes with a hierarchical pore structure, as they are either overly-simple (e.g., an RC circuit) [20], consist of transmission line or ladder network representations of porous electrodes with unimodal, non-hierarchical pore structure [3,21,22], or capture the effects of a continuous pore size distribution of parallel pores [23]. Surprisingly, despite the widespread development of hierarchical porous electrode capacitors and their frequent characterization by EIS [24–27], few previous studies interpreted their EIS results using circuit models specifically for hierarchical electrodes. Exceptions include the work by Eikerling et al. and Yoon et al. [19,28]. Eikerling et al. presented a circuit model capturing the impedance of a hierarchical electrode consisting of an amalgamation of porous carbon agglomerates [19]. Yoon et al. described a model capturing the impedance of templated hexagonal mesoporous carbon electrodes [28]. However, each of these ad hoc circuit models was material specific and complex. For example, the model of Eikerling et al. captures the impedance of a multi-scale pore structure within the carbon agglomerates by using a complex self-affine Cantor-block model [19]. Further, in these works, limited experimental results were presented. The work of Eikerling et al. and Yoon et al. each presented EIS results from a single electrode material with varying electrode thickness [19,28].

We here present a combined theory (linear circuit model) and experimental (EIS) study using a set of newly-developed hierarchical carbon aerogel monolith (HCAM) electrodes which have a bimodal pore size distribution. These electrodes have been applied successfully to energy storage [29,30], and water desalination systems [7]. HCAM electrode materials are fabricated initially with a continuous micron-scale pore network. Nanoscale features are then etched into the surfaces of this network by thermal activation [31]. The set of electrodes we use in this study includes both unactivated samples and activated samples with varying activation times (time the sample is exposed to a high temperature CO_2 environment). By tuning the activation time, we can controllably vary the pore structure of our hierarchical electrode, and study the effects of this alteration on measured impedance. Additionally, we present and analyze a simple circuit model representing a hierarchical electrode with strongly bimodal porosity (i.e. with nanoscale pores integrated into a micron-scale pore network). Our combined model and experimental results allow us to demonstrate the utility of our model, provide detailed characterizations of our HCAM electrode set, study the effect of pore structure variations on electrode impedance, and present guidelines toward hierarchical electrode design and characterization. We further show evidence suggesting our techniques can enable the detailed study of hierarchical electrodes with sub-nanometer (sub-nm) diameter pores, where sub-nm pores have generated significant interest for enabling high energy density electrochemical capacitors [32,33].

2. Theory

We here present a linear circuit model representing the impedance of a hierarchical porous electrode with bimodal porosity. The model represents a morphology where smaller nanometer or sub-nm scale "storage" pores are integrated into the surfaces of a network of larger "transport" pores. We build our circuit model based on the idealized structure shown in Fig. 1a: A finite length transport pore with an amount m of smaller, branching storage pores equally distributed along the length of the transport pore. Consistent with traditional and widely-used assumptions for porous electrode impedance models [3,19,21], we model each of the two sets of pores as having a uniform cross-section; we assume negligible resistance of the electrode solid phase; and we assume that the pores are completely filled with a uniform electrolyte. As per Fig. 1b, we model the hierarchical pore impedance, Z, as a distributed network of the transport pore electrolyte resistance, $R_{t,1}$, and the transport pore wall impedance, $Z_{w,1}$ [21,34]:

$$Z = \left(R_{t,1}Z_{w,1}\right)^{1/2}\coth\left[\left(R_{t,1}/Z_{w,1}\right)^{1/2}\right]. \quad (1)$$

In our notation, the first subscript denotes a property of the transport pore, "t", the transport pore wall, "w", or of the storage pore, "s". With the second subscript, we denote either a property of a single pore, "1", or the effective property of "m" pores in parallel. In Eq. (1), $R_{t,1}$ and $Z_{w,1}$ are each in units of Ohms. We describe $Z_{w,1}$ as a parallel combination of the EDL capacitance of the transport pore wall, $C_{t,1}$, and the impedance of the m branching storage pores, $Z_{s,m}$:

$$Z_{w,1} = \frac{Z_{s,m}j}{j - \omega C_{t,1}Z_{s,m}}. \quad (2)$$

Here, ω is the angular frequency of the input signal and j is the unit imaginary number. We further model each individual storage pore as a distributed network of the storage pore electrolyte resistance,

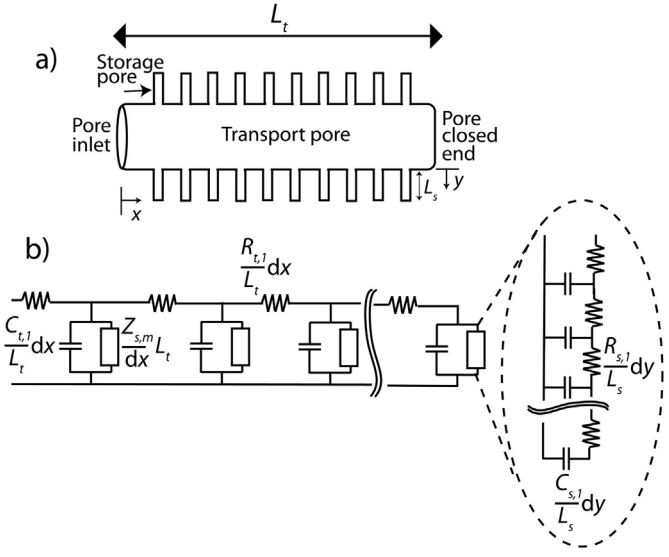

Fig. 1. a) Schematic of a single, finite length transport pore with a number m of equally spaced, branching storage pores. b) The circuit model used to describe the impedance of the structure shown in a). This impedance consists of a distributed network of the transport pore resistance, $R_{t,1}$, and the transport pore wall impedance, $Z_{w,1}$. $Z_{w,1}$ is a parallel combination of the transport pore EDL capacitance, $C_{t,1}$, and the impedance attributed to the m storage pores $Z_{s,m}$. Within the dotted lines, we show the circuit model representing the impedance of a single storage pore, which is a distributed network of that pore's resistance, $R_{s,1}$ and capacitance, $C_{s,1}$.

$R_{s,1}$, and the storage pore's EDL capacitance, $C_{s,1}$ (see Fig. 1b). The impedance associated with the m storage pores, $Z_{s,m}$, is then [34]:

$$Z_{s,m} = (1-j)\left(\frac{R_{s,m}}{2\omega C_{s,m}}\right)^{1/2}\coth\left[(1+j)\left(\omega R_{s,m}C_{s,m}/2\right)^{1/2}\right], \quad (3)$$

where $R_{s,m}$ is the total resistance associated with all the storage pores lining the transport pore wall ($R_{s,m} = R_{s,1}/m$), and $C_{s,m}$ is total capacitance contributed by storage pores ($C_{s,m} = mC_{s,1}$). Thus, Eqs. (1)–(3) describe the impedance of our hierarchical pore using four parameters, $R_{t,1}$, $R_{s,m}$, $C_{t,1}$ and $C_{s,m}$. The model for a pore is extended to that of an electrode by approximating the electrode pore structure as many, non-intersecting, hierarchical pores in parallel. To model the electrode, we use Eqs. (1)–(3) but replace $R_{t,1}$ with R_t, the electrode resistance associated with transport pores ($R_t = R_{t,1}/n$, where n is the number of parallel transport pores in the electrode), $R_{s,m}$ with R_s, the electrode resistance associated with storage pores ($R_s = R_{s,1}/(nm)$), and $C_{t,1}$ and $C_{s,m}$ with C_t and C_s respectively ($C_t = nC_{t,1}$, $C_s = nmC_{s,1}$).

Our intent with this four-parameter representation is to construct a model which is as simple as possible but still captures some of the complexity of an electrode with hierarchical and bimodal pore structure. Electrodes which instead consist of porous carbon agglomerates, where the agglomerates' internal pore structure has several scales for pore size, may require more complex multi-scale or continuous-scale models, as presented by, for example, Eikerling et al. [19]. The models of Yoon et al. and Bazant describe the impedance of a hierarchical electrode with bimodal porosity, but do not account for the transport pore capacitance as we do here [28,35]. As we demonstrate in Supplementary information, Section 1, the transport pore capacitance is an important parameter in describing the impedance of hierarchical, bimodal electrodes. We note that the resistance of the nanoscale storage pores, R_s, can potentially be affected by many parameters such as specific pore topology, pore surface charge, and surface chemistry [9,36,37]. In our model, we cannot individually resolve these effects.

In Fig. 2, we plot the complex impedance given by Eqs. (1)–(3), for an example case of $C_s = 1$ F, $C_t = 0.01$ F, $R_t = 1\ \Omega$, and for selected values of R_s ranging from $R_s = 0.001R_t$ to $10R_t$ (see Fig. 2 caption for legend). Impedance is plotted for an input frequency range of 100 kHz to 50 mHz, where 100 kHz corresponds to the point closest to the origin of each curve, and the magnitude of impedance increases with decreasing frequency. Here, we choose $C_s >> C_t$ to reflect the significantly higher surface area associated with storage pores in typical hierarchical electrodes. Further, we scale the real axis by $R_t/3$ and the imaginary axis by $1/(\omega_f C_s)$, where ω_f is 2π(50 mHz). The real axis scaling is motivated by the observation that the total electrode resistance is thrice the real axis asymptote value [34,38]. The imaginary axis is scaled by the magnitude of the impedance of a planar capacitor with capacitance C_s at frequency ω_f. In Fig. 2, we note several differences between impedance curves for the case of small R_s ($R_s << R_t$), and those with significant R_s. For small R_s, $R_s = 0.001R_t$ and $0.01R_t$, the electrode impedances are approximately equal at all frequencies. The impedance curves for low R_s values are characterized by a 45° phase angle at higher frequencies, and a real axis asymptote at the lowest frequencies (to a value of unity on the scaled x-axis). The 45° phase angle and real axis asymptote are features commonly associated with the impedance of finite length porous electrodes [19,34]. Also, the real axis asymptote of unity indicates that the total resistance of the hierarchical electrode is approximately that of the transport pores, R_t. On the other hand, when R_s is within an order of magnitude of R_t or greater, $R_s \geq 0.1R_t$, we observe that impedance curves vary significantly for different values of R_s, the phase angle at higher frequencies departs significantly from 45°, and the real axis asymptote is higher than unity and increases with R_s. For example, for the case where $R_s = R_t$, the phase angle is approximately 22.5° for frequencies below 1 Hz. Also, for $R_s = R_t$, the x-axis asymptote is 2, indicating that the total resistance of the electrode is $2R_t$, consistent with the increasing importance of the resistance of the storage pores.

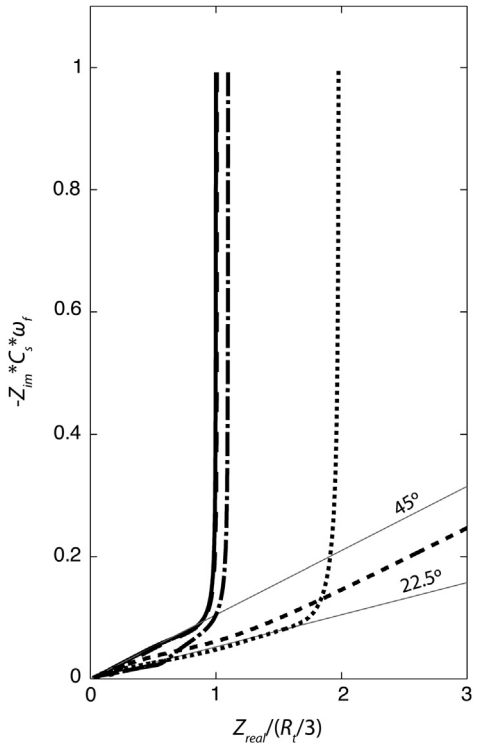

Fig. 2. Nyquist plot of the impedance of a hierarchical electrode with bimodal pore size distribution. The real axis is scaled by $R_t/3$, and the imaginary axis by $1/(\omega_f C_s)$. We plot the impedance for a frequency range of 50 mHz–100 kHz, $C_s = 1$ F, $C_t = 0.01$ F, $R_t = 1\ \Omega$, and $R_s = 0.001R_t$ (black line), $0.01R_t$ (long dashes), $0.1R_t$ (dash-dot), R_t (dot), and $10R_t$ (short dashes). The impedances for $R_s = 0.001$ and $0.01R_t$ are approximately the same for all frequencies, and so these curves are largely indistinguishable in the plot. For the case of small R_s, $R_s \leq 0.01R_t$, impedance curves are independent of R_s, have a 45° phase angle at higher frequencies, and asymptote to a value of approximately unity on the real axis. For non-negligible R_s, $R_s \geq 0.1R_t$, impedance varies strongly with R_s, the phase angle at high frequencies is significantly lower than 45°, and the real axis asymptote is greater than unity and increases with R_s.

We make several important observations from our model results for the (common) case where $C_s >> C_t$. First, small R_s ($R_s << R_t$) is desired for device operation, as here the storage pores can add significant capacitance and system performance but negligible resistance. In this regime, further minimization of electrode ionic resistance can only occur by decreasing transport pore resistance, R_t. For the case of significant R_s relative to R_t, storage pores add significantly to overall electrode ionic resistance, and so both R_s and R_t are important parameters governing electrode performance. Second, the model suggests that impedance measurements can be used to quickly characterize whether a given electrode material has a small or large R_s. This can be ascertained by observing the phase angle at higher frequencies; if this angle is about 45°, then R_s is small (relative to R_t), but if the angle is instead significantly less than 45°, this indicates that R_s may be non-negligible. Third, the model given by Eqs. (1)–(3) potentially allows for detailed characterizations of hierarchical electrodes, as by fitting this model to experimental data, we can potentially extract

both the capacitance and resistance associated with solely storage pores and also that associated with solely transport pores.

As noted by de Levie, the phase angle observed at high frequencies (where the pore can be considered semi-infinite) is half that of the pore wall impedance [34]. Thus, for a hierarchical pore with small R_s, the 45° phase angle shown in our model results indicates that in this case the wall impedance can be approximated by a capacitor. It is thus possible to simplify the model given in Eqs. (1)–(3), for the case $R_s << R_t$, to the following:

$$Z = (1-j)\left(\frac{R_t}{2\omega C_s}\right)^{1/2} \coth\left[(1+j)(\omega R_t C_s/2)^{1/2}\right]. \quad (4)$$

In Eq. (4), we represent our hierarchical pore by a transmission line circuit where the wall impedance is simply the capacitor C_s (we assumed $C_s >> C_t$). This model contains only two parameters, R_t and C_s, and can be used to fit to EIS data from well-designed (ideal) hierarchical electrodes (with $R_s << R_t$ and $C_s << C_t$).

3. Experimental methods

To further explore the impedance of hierarchical porous carbon electrodes with bimodal porosity, we ran EIS experiments on a set of hierarchical carbon aerogel monolith (HCAM) electrodes. Importantly, we varied the pore structure of our electrodes in a controlled manner *via* use of thermal activation and variations of thermal activations times [31]. This allowed us to, for the first time, study the effect of pore structure variations on measured impedance of capacitive hierarchical electrodes.

3.1. Electrode fabrication

Our electrodes were prepared as described in detail by Baumann et al. [31], and so we will only summarize preparation details here. The aerogels were fabricated using the sol–gel polymerization of resorcinol with formaldehyde, and with acetic acid as a catalyst. The use of acetic acid catalyst enabled the formation of an interconnected micron-scale pore network which served as transport pores [31]. This base, or unactivated, material was then cut into several slabs, one of which was left unactivated, and the remaining slabs each underwent treatments of thermal activation in CO_2 at 950 °C for varying times including 2, 4 and 5.5 h. The activated and unactivated aerogels used in EIS measurements were all cut into approximately 5.5 × 5.5 × 1 mm pieces using a Dremel tool (Dremel, Racine, WI). This latter set of cut electrodes was used in our EIS measurements.

3.2. Electrode pore structure characterization

We acquired scanning electron microscopy (SEM) images of our porous carbon electrodes to characterize the effect of thermal activation on the transport pore network. Fig. 3 shows SEM images for an unactivated sample and a thermally activated sample at the same imaging scale. To create the two samples shown in Fig. 3, an unactivated slab was cleaved into two parts, one of which was thermally activated for 5 h and the other remained unactivated. SEM characterization was performed on a JEOL 7401-F (Peabody, MA) at 5–10 keV in secondary electron imaging mode with a working distance of 2–8 mm. Sample dimensions were roughly 10 × 10 × 1 mm. Due to the high electrical conductivity of the carbon aerogels, conductive coating of samples was not required for SEM imaging. In Fig. 3a, we show the SEM image of the unactivated sample's micron-scale pore network (see Supplementary information, Section 2 for higher magnification SEM images). In Fig. 3b, we show the micron-scale pores of the activated sample, and observed a modified micron-scale pore network including larger micron-scale pores and a more open pore structure characterized by sub-micron features and sharper edges. Note the higher density of features including thin carbon ligaments.

Fig. 4 shows the results our N_2 adsorption measurements as incremental pore volume *vs.* pore size for various HCAM samples. These measurements serve to characterize the storage pore size distribution of our electrodes. The N_2 adsorption isotherms were measured with an ASAP 2020 Surface Area Analyzer (Micromeritics Instrument Corporation). Samples of approximately 0.2 g were heated to 300 °C under vacuum (10^{-5} Torr) for at least 24 h to remove adsorbed species, and nitrogen adsorption data were then collected at relative pressures from 10^{-7} to 0.3 at 77 K. The pore size distributions were calculated using Micromeritics DFTPlus v3.01 software. As seen in Fig. 4, the unactivated material's storage pores are largely sub-1 nm (thick line with squares). The total (cumulative) volume associated with the storage pores in the unactivated material is 0.094 $cm^3\ g^{-1}$. Upon thermal activation for 2 h, the total volume associated with the nanoscale pores increases significantly to 0.58 $cm^3\ g^{-1}$ (thin line with diamonds), and then increases further to 0.99 $cm^3\ g^{-1}$ at 5.5 h activation (thin line with right pointing triangle). Further, for samples activated longer than 2 h, the majority of the measured volume is attributed to pores of between 1 and 3 nm. The maximum measured storage pore size increases from ~1 nm on the unactivated sample to nearly 3 nm for the 5.5 h activated sample.

We also measured electrode porosity through dry/wet measurements of electrode mass. The electrode was weighed dry, then

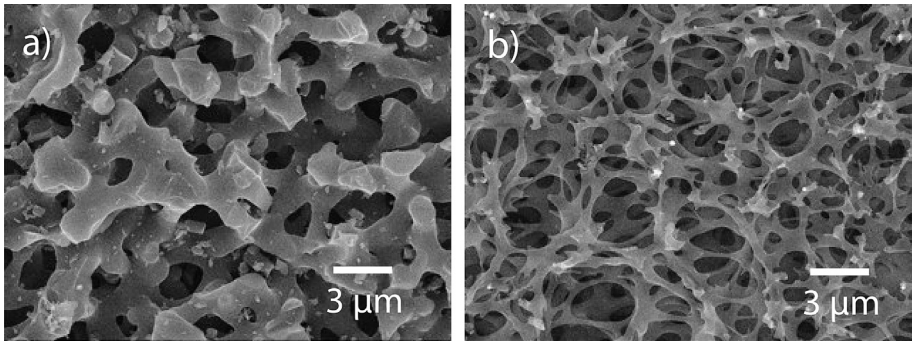

Fig. 3. SEM images used to characterize the transport pore network of our HCAM electrodes. a) An SEM image of an unactivated HCAM sample and b) of a 5 h activated HCAM sample. We observed that both the unactivated and the activated material possess a transport pore network with order 1 μm pores. Comparing images a) and b), we observe qualitatively that activation enlarges micron-scale transport pores and results in a finer-scale network of connected, thin carbon ligaments.

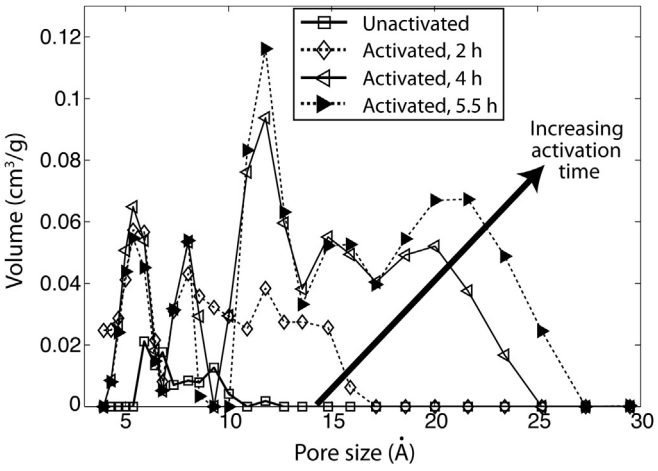

Fig. 4. Results of N_2 adsorption measurements used to measure the storage pore size distribution of our HCAM electrode set. Results are plotted as incremental pore volume *vs.* pore size. The volume measured for the unactivated sample is contained nearly exclusively in sub-nm pores, while that of the samples activated for over 2 h is largely attributed to 1–3 nm pores. The total measured storage pore volume is 0.094 $cm^3\ g^{-1}$ for the unactivated sample, and increases significantly upon thermal activation to 0.99 $cm^3\ g^{-1}$ for the 5.5 h activated sample.

was infiltrated with DI water by sonication for 10 min (FS30 Ultrasonic Cleaner, Fisher Scientific, Waltham, MA). Water was removed from the wet electrode surface using a Kimwipe (Kimberly-Clark, Neenah, WI), and the electrode was then weighed again. The porosity of our unactivated electrode was 0.60 and that of our 5.5 h activated electrode 0.81, consistent with a significant increase in void volume due to thermal activation.

3.3. EIS measurements

We performed EIS measurements in a three-electrode setup with an Ag/AgCl reference electrode (Fisher Scientific, Waltham, MA) and Pt foil counter electrode (Alfa Aesar, Ward Hill, MA). In Fig. 5, we depict our custom-fabricated working electrode setup. Here, we held the HCAM sample between two 2 × 2 cm Teflon plates (McMaster-Carr, Robbinsville, NJ). The front Teflon plate (facing the reference and counter electrode) had a 5 × 5 mm window laser ablated into its center (Universal Laser Systems, Scottsdale, AZ). A 5 × 0.5 cm sheet of Pt foil was placed between the rear Teflon plate and the HCAM sample. The top part of this foil was connected to the working electrode lead from our potentiostat (Bio-Logic, Claix, France), and the Pt foil served to apply voltage uniformly along the backside of the HCAM sample. A compressible Teflon gasket (Gore, Newark, DE) was placed between the two Teflon plates to seal the perimeter of the working electrode setup. A 3 × 5 cm piece of Pt foil served as the counter electrode. The working, reference, and counter electrodes were inserted into a glass beaker which was filled with the sodium chloride solution of interest. After inserting the working electrode into the cell, we waited 1 h before performing experiments to allow for the cell to equilibrate with the sodium chloride solution. EIS experiments were performed in 0.5 and 2.5 M NaCl, where the 2.5 M results are reported here, and the 0.5 M results served as a good comparison case and are discussed in Supplementary information, Section 3. Before each EIS experiment, we set the working electrode voltage with our potentiostat (from 0.5 to −0.5 V *vs.* Ag/AgCl), and then waited at least 10 min for the system to approach equilibrium (for current to approach approximately zero). Due to the use of high concentration NaCl, we expected no significant desalination (concentration gradients) in the transport pores of our electrode upon application of the working electrode voltage. During EIS experiments, we applied potential perturbations of amplitude 5 mV, and scanned over a frequency range of 10 kHz–10 mHz.

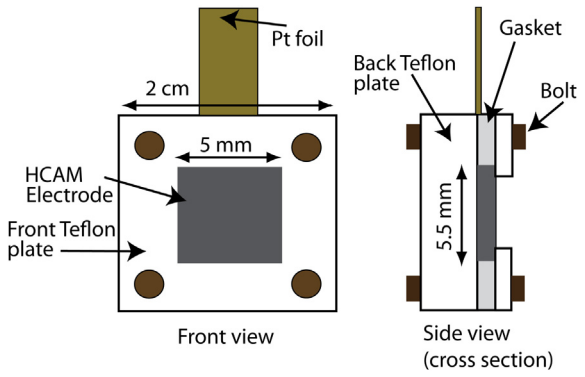

Fig. 5. Schematic of the working electrode setup used in EIS measurements. The 5.5 × 5.5 × 1 mm HCAM electrode is held in compression between two Teflon plates. A window cut into the front Teflon plate allows for ionic current to enter and exit the HCAM pore structure. A sheet of platinum foil pressed against the backside of the HCAM electrode served as a current collector, and was connected to the potentiostat working electrode lead.

4. Experimental results

In Fig. 6, we show the results of our EIS measurements on our set of HCAM electrodes. The electrodes were held at a potential of 0 V with respect to our Ag/AgCl reference electrode, and we applied a 5 mV amplitude sinusoidal voltage perturbation with a frequency range of 10 kHz–10 mHz. The impedance data is plotted as the real component of impedance, Z_{real}, subtracted by the series resistance, R_{ser}, *vs.* the negative of the imaginary component of impedance, $-Z_{im}$ (the black dots in Fig. 6). R_{ser} is the (real) impedance measured at 10 kHz, and represents the total resistance of the

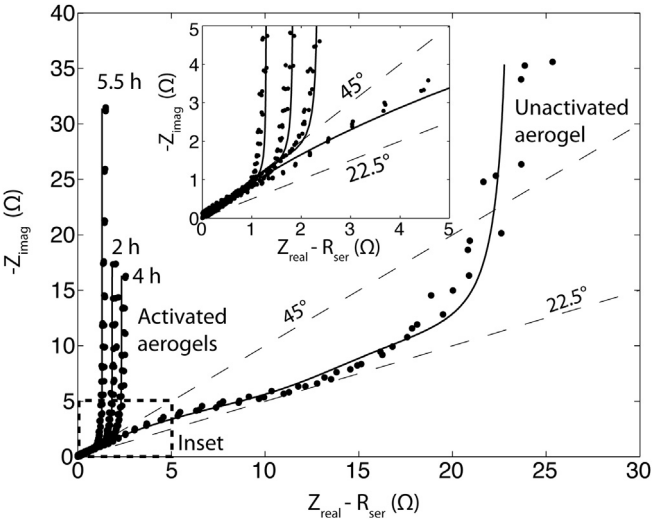

Fig. 6. EIS measurements of unactivated, and several activated HCAM electrodes with varying activation times. Inset shows a close-up of the near origin section of the figure. Measurements were taken at 0 V *vs.* Ag/AgCl, with a 5 mV amplitude, and with a frequency range from 10 kHz to 10 mHz. The black dots are the experimental data, and the curves are the fitted circuit model results (using the model described in the Theory section). The unactivated HCAM electrode exhibits a relatively large real axis asymptote of approximately 25 Ω, and a sub-45° phase angle at higher frequencies. The activated electrodes exhibit a constant 45° phase angle at higher frequencies, and a relatively low valued real axis asymptote of less than 3 Ω.

measurement system which is not associated with the porous HCAM material. For each material, the impedance data nearest to the origin (the black dot nearest to the origin) is the impedance measured at the highest perturbation frequency, and as frequency is lowered, the magnitude of the impedance increases. For each sample, we show three sets of data representing three consecutive frequency sweeps.

Fig. 6 shows EIS data for all four HCAM electrode activation levels: unactivated and 2, 4, and 5.5 h activated. For the three activated electrodes, we observed a measured impedance distribution with an approximate 45° phase angle for frequencies above about 1 Hz (see Fig. 6 inset for close-up of the high frequency data), and a real axis asymptote at lower frequencies. Slight variations in the impedance of the activated samples were also observed, as both the real axis asymptote, and the magnitude of the imaginary component at the lowest frequency varied between activated samples. For example, the real axis asymptote for the 5.5 h electrode was about 1.5 Ω, compared to a value of about 2.5 Ω for the 4 h activated sample. The latter variation reflects the difference in resistance between the activated electrodes, and will be discussed further in Table 1 and associated text. In contrast to the activated HCAM samples, the unactivated HCAM material exhibited markedly different impedance characteristics. At high frequencies (above 100 Hz), the phase angle was roughly 45°, and phase angle decreased to 22.5° at intermediate frequencies (1–0.1 Hz). At the lowest frequencies of the order of 10 mHz, the value of $Z_{real} - R_{ser}$ asymptoted to about a value of roughly 25 Ω.

We now offer an interpretation for the key characteristics we observe in the measured impedances of our HCAM electrode set. We make this interpretation in light of the trends suggested by the circuit model described in the Theory section, and based on the porosimetry measurements described in the Experimental methods section. Firstly, the measured impedance of our three hierarchical activated electrodes all demonstrate characteristics consistent with negligible storage pore resistance, R_s ($R_s << R_t$): All three electrodes show a 45° phase angle at higher frequencies, and a relatively small real axis asymptote of about 1.5–2.5 Ω. Secondly, the measured impedance of the unactivated HCAM sample demonstrates the characteristics expected of a hierarchical electrode with significant R_s. That is, the unactivated material demonstrates a phase angle significantly less than 45° (approaching 22.5°) at higher frequencies, and a relatively large real axis asymptote of about 25 Ω. The porosimetry results shown in Fig. 4 support our contention that a significant lowering of R_s occurs upon activation. These results showed a nearly order of magnitude jump in gravimetric storage pore volume (from 0.094 to 0.58 $cm^3\ g^{-1}$) between the unactivated and 2 h activated HCAM sample. This data indicates that thermal activation creates a significant amount of new nanometer scale features (new storage pores), consistent with previous published descriptions of the effect of thermal activation on carbon surfaces [31,39]. Further evidence of the creation of new nanoscale features upon thermal activation can be seen in the SEM images of Supplementary information, Section 2. As R_s is the resistance of all storage pores in parallel ($R_s = R_{s,1}/[n \times m]$, see Theory section), increasing the number of storage pores is expected to reduce R_s.

To further characterize our materials and demonstrate the model efficacy, we fit the EIS data shown in Fig. 6 to the circuit model developed in the Theory section. We fit the unactivated HCAM data to the circuit model given by Eqs. (1)–(3), and the activated data to the simplified model valid for $R_s << R_t$, $C_s >> C_t$ given by Eq. (4). To perform these fits, we used a custom, non-linear least squares fitting algorithm coded in Matlab (using the function *lsqnonlin*) which minimized the sum of the imaginary and real squared errors. We used four fitting parameters for the unactivated data (R_s, R_t, C_s, C_t), and two for the activated data (R_t, C_s). In Fig. 6 we show the fitted circuit model results as black curves, and these curves closely follow the EIS data (black dots) for all four HCAM samples. The root mean square error for the activated samples was 0.0046, 0.0048, and 0.0054 Ω for the 2, 4, and 5.5 h activated samples, respectively, and 0.029 Ω for the unactivated sample. In Table 1, we tabulate the parameters extracted from fitting the data with our model. We normalized extracted capacitance by the dry electrode mass and the extracted resistance by the electrode thickness in the electric field direction/electrode cross sectional area to obtain resistivity. As shown in Table 1, for the unactivated electrode, the resistivity of the storage pores, ρ_s, is measured to be 150 Ω cm, slightly higher than the 110 Ω cm measured for the transport pores. Further, we measure a much higher capacitance associated with the storage pores (46 F g^{-1}) than with the transport pores (2.5 F g^{-1}). The latter result is expected, as we estimate that the unactivated material's transport pores have a surface area of less than 10 $m^2\ g^{-1}$, while that of the storage pores is several hundred $m^2\ g^{-1}$ [31]. We also measured a significant drop in resistivity associated with the transport pores, ρ_t, upon activation. For example, ρ_t drops by a factor of about 5 from the unactivated to the HCAM sample activated for 2 h. We attribute this drop to the observed etching out of the transport pore network upon thermal activation (see Fig. 3), which increases the porosity and likely decreases the tortuosity (effective length) of the pore structure (see Experimental methods section for porosity measurements). Table 1 also shows that the gravimetric capacitance of the thermally activated samples (85–113 F g^{-1}) is significantly higher than that of the unactivated sample (46 F g^{-1}), consistent with the significant increase in the amount of storage pores upon thermal activation. As we increase activation times from 2 to 5.5 h, we measure a monotonic decrease in ρ_t from 20.4 to 14.4 Ω cm, and a monotonic increase in C_s from 85 to 113 F g^{-1} at 5.5 h activation time. Note that in Fig. 6, the resistance of the 2 h activated sample is less than that of the 4 h activated sample (i.e. the real axis asymptote of the 2 h sample is smaller than that of the 4 h sample). On the other hand, as per Table 1, the resistivity value, ρ_t, of the 2 h sample is higher than the 4 h sample. The difference between resistance and resistivity trends is due to a small difference in the geometries of our Dremel-cut samples, where the 4 h activated sample had a slightly greater thickness than the 2 h sample.

In Fig. 7a and b, we show the results of EIS measurements of the 2 h activated and unactivated HCAM, respectively, but here we perform EIS with the electrode held at potentials varying from −0.5 to 0.5 V *vs.* Ag/AgCl. In the inset of b), we show a close-up of the near-origin region of Fig. 7b. As seen in Fig. 7a, the activated material exhibits a largely voltage-independent impedance, as all impedance data approximately collapses along a single curve. In contrast, as shown in Fig. 7b, the unactivated material exhibits a strongly voltage dependent impedance. For the unactivated HCAM, at 0 V (black dots in Fig. 7b) and −0.1 V (right facing triangles in Fig. 7b), we note the high $Z_{real} - R_{ser}$ asymptote and the

Table 1
Parameters extracted from the model to data fits shown in Fig. 6. ρ is the resistivity and C is the gravimetric capacitance, while the subscripts t and s refer to transport or storage pores, respectively. Comparing the unactivated electrode to the 2 h activated electrode, we see a drop in ρ_t from 110.1 to 20.4 Ω cm, a drop in ρ_s from 150.0 Ω cm to a negligible value, and an increase in C_s from 46 to 85 F g^{-1} upon activation. As we activate for longer times, ρ_t decreases monotonically and C_s increases monotonically.

	ρ_t [Ω cm]	ρ_s [Ω cm]	C_t [F g^{-1}]	C_s [F g^{-1}]
Unactivated	110.1	150.0	2.5	46
Activated (2 h)	20.4	–	–	85
Activated (4 h)	17.7	–	–	110
Activated (5.5 h)	14.4	–	–	113

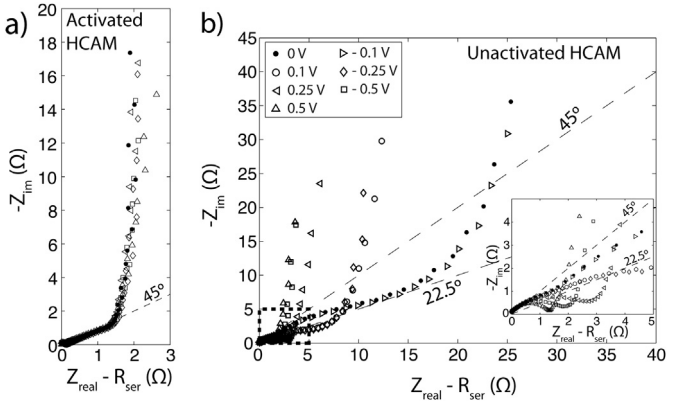

Fig. 7. Results of EIS measurements on the a) HCAM electrode activated for 2 h and for b) the unactivated HCAM electrode. Both electrodes were held at various applied potentials from −0.5 to 0.5 V *vs.* Ag/AgCl (legend in b applies to both a and b). Inset in b) shows a close-up of the near-origin region of b denoted as a dashed box. In a) we observed that the activated electrode had an impedance that was largely voltage independent. In contrast, in b) the measured impedance of the unactivated electrode shows a significant voltage-dependence. At low voltages of 0 and −0.1 V, the impedance of the unactivated sample is about that shown in figure, with a relatively large *x*-axis asymptote value, and a sub 45° phase angle at higher frequencies. At higher voltages, the impedance curves change drastically, as the *x*-axis asymptote and the imaginary component of the impedance at the lowest frequency (10 mHz) both decrease significantly. Further, at high voltages, a semi-circle feature appears at high frequencies over order 1 Hz (see inset).

approximately 22.5° phase angle at intermediate frequencies. As voltage magnitude is increased, we observe a lowering of the $Z_{real} - R_{ser}$ asymptote value, and a decrease in the magnitude of Z_{im} at the lowest frequency (10 mHz). At high voltages, we further note the presence of new features in the high frequency impedance (see inset). For example, at 0.5, −0.5, and 0.25 V, we observe a semi-circle-like feature spanning frequencies from 10 kHz to order 1 Hz.

We hypothesize that the strong voltage dependence of the unactivated HCAM's impedance is due to the sub-nm size of the storage pores on this material (see Fig. 4). Chmiola et al. and Segalini et al. previously demonstrated that electrodes with sub-nm pores can exhibit high specific capacitance, and attributed this to distortion of the ion's solvation sheath as it enters the charging pore [32,40]. Recently, molecular dynamics simulations have demonstrated that this phenomenon can be strongly voltage dependent [33]. That is, at low electrode voltages ions can be sterically excluded from sub-nm pores, but at higher voltages, the ion solvation sheath can distort allowing ion entry to be possible [33]. Thus, for a hierarchical electrode with sub-nm storage pores, we may expect a strong potential-dependence of its impedance. More specifically, we might expect an increase in measured storage pore capacitance, C_s, and decrease in resistance associated with storage pores, R_s, as voltage increases (as a higher number of storage pores can accept ions). From the data in Fig. 7b and calculations described in Supplementary information, Section 4, the measured resistance of the unactivated electrode indeed decreased from 73.9 to about 10 Ω and the measured capacitance increased from 48.5 to approximately 92 F g^{-1} as the voltage increased from 0 V to 0.5 V (or decreased to −0.5 V). We note that the circuit model presented in the Theory section must be modified to fit the entire frequency spectrum of the high voltage data in Fig. 7b, as our model does not capture the distinct semi-circular feature seen at high frequencies (Fig. 7b inset). We present possible ameliorations to our circuit model in Supplementary information, Section 4, and show that including transport limitations for ions entering sub-nm storage pores can result in semi-circular features in the model impedance. The previous discussion highlights the potential of our combined model and experimental approach as a first step toward detailed, quantitative, EIS-based studies of the voltage-dependent mechanisms governing sub-nm pore charging in hierarchical electrodes. We also note that high-frequency semi-circle type features have been observed in EIS studies of metal oxide pseudocapacitive electrodes, where these features are attributed to electrochemical reactions [41]. While carbon aerogel electrodes are typically not associated with pseudocapacitive-type ion storage mechanisms (without additional chemical treatments or insertion of metal oxide particles) [42], we believe further study is still required to conclusively exclude this explanation. Lastly, we note that an alternative explanation for our observation of increased unactivated HCAM electrode capacitance with increased bias voltage is an increase in the carbon's density of electronic states [43]. However, the latter phenomena does not, to our knowledge, account for the observed decrease in unactivated HCAM electrode's resistance with bias voltage (see Fig. 7).

5. Conclusion

Hierarchically-structured porous carbon electrodes are commonly used in energy storage, energy harvesting, and water desalination applications. We here presented an impedance-based theory and experimental study of hierarchical porous electrodes with bimodal porosity (with nanoscale pores integrated into a micron-scale pore network). We developed and analyzed a linear circuit model, and this model is generally applicable to electrodes with the latter pore structure. Using EIS, we measured the impedance of a set of hierarchical carbon aerogel monolith (HCAM) materials. In this set, we controllably varied the electrode's pore structure by varying thermal activation time. Combining the theory and experiments, we performed detailed characterizations of our HCAM electrode set, studied the effect of pore structure variations on electrode impedance and performance, and demonstrated the utility of our model. Further, we measured a strongly voltage dependant impedance of our unactivated HCAM material, which we attributed to the charging of the sub-nanometer storage pores of this material.

Acknowledgments

This work was supported by the National Science Foundation under grant no. 0967600 and State of California's Proposition 50 funds administered by the Department of Water Resources. Any opinions, findings, and conclusions or recommendations expressed in this material are those of the authors and do not necessarily reflect the views of the National Science Foundation. MES would like to thank the Lawrence Scholar program and a postgraduate scholarship from the Natural Sciences and Engineering Research Council (NSERC) of Canada. Work at LLNL was performed under the auspices of the US DOE by LLNL under Contract DE-AC52-07NA27344. We would like to thank Kendra Kuhl, Benjamin Reinecke, Zhebo Chen, and Etosha Cave for their training and technical assistance in the use of three-electrode cells and the potentiostat.

Appendix A. Supplementary data

Supplementary data related to this article can be found at http://dx.doi.org/10.1016/j.jpowsour.2013.03.178.

References

[1] J.C. Farmer, D.V. Fix, G.V. Mack, R.W. Pekala, J.F. Poco, Journal of the Electrochemical Society 143 (1996) 159–169.
[2] D. Brogioli, Physical Review Letters 103 (2009) 058501.
[3] R. Kotz, M. Carlen, Electrochimica Acta 45 (2000) 2483–2498.

[4] B.E. Conway, Electrochemical Supercapacitors, Kluwer Academic/Plenum Publishers, New York, 1999.
[5] D. Brogioli, R. Zhao, P.M. Biesheuvel, Energy & Environmental Science 4 (2011) 772–777.
[6] B.B. Sales, M. Saakes, J.W. Post, C.J.N. Buisman, P.M. Biesheuvel, H.V.M. Hamelers, Environmental Science & Technology 44 (2011) 5661–5665.
[7] M.E. Suss, T.F. Baumann, W.L. Bourcier, C.M. Spadaccini, K.A. Rose, J.G. Santiago, M. Stadermann, Energy & Environmental Science 5 (2012) 9511–9519.
[8] P.M. Biesheuvel, A. van der Wal, Journal of Membrane Science 346 (2010) 256–262.
[9] P.M. Biesheuvel, M.Z. Bazant, Physical Review E 81 (2010) 031502.
[10] Y. Oren, Desalination 228 (2008) 10–29.
[11] S. Porada, L. Weinstein, R. Dash, B. van der Wal, M. Bryjak, Y. Gogotsi, M. Biesheuvel, ACS Applied Materials & Interfaces (2012).
[12] P. Simon, Y. Gogotsi, Nature Materials 7 (2008) 845–854.
[13] T. Humplik, J. Lee, S.C. O'Hern, B.A. Fellman, M.A. Baig, S.F. Hassan, M.A. Atieh, F. Rahman, T. Laoui, R. Karnik, E.N. Wang, Nanotechnology 22 (2011) 292001–292019.
[14] C.N. Satterfield, C.K. Colton, W.H. Pitcher, AIChE Journal 19 (1973) 628–635.
[15] P.M. Biesheuvel, Y. Fu, M.Z. Bazant, Physical Review E 83 (2011) 061507.
[16] D.-W. Wang, F. Li, M. Liu, G.Q. Lu, H.-M. Cheng, Angewandte Chemie 120 (2008) 379–382.
[17] C. Tsouris, R. Mayes, J. Kiggans, K. Sharma, S. Yiacoumi, D. DePaoli, S. Dai, Environmental Science & Technology 45 (2011) 10243–10249.
[18] Z.Y. Yuan, B.L. Su, Journal of Materials Chemistry 16 (2005) 663–677.
[19] M. Eikerling, A.A. Kornyshev, E. Lust, Journal of the Electrochemical Society 152 (2005) E24–E33.
[20] P.L. Taberna, P. Simon, J.F. Fauvarque, Journal of the Electrochemical Society 150 (2003) A292–A300.
[21] R. de Levie, Electrochimica Acta 8 (1963) 751–780.
[22] R.A. Dougal, L. Gao, S. Liu, Journal of Power Sources 126 (2004) 250–257.
[23] H.-K. Song, H.-Y. Hwang, K.-H. Lee, L.H. Dao, Electrochimica Acta 45 (2000) 2241–2257.
[24] G. Sun, W. Song, X. Liu, W. Qiao, D. Long, L. Ling, Journal of Solid State Electrochemistry 16 (2012) 1263–1270.
[25] H. Yamada, H. Nakamura, F. Nakahara, I. Moriguchi, T. Kudo, The Journal of Physical Chemistry C 111 (2006) 227–233.
[26] D.-W. Wang, F. Li, H.-M. Cheng, Journal of Power Sources 185 (2008) 1563–1568.
[27] P. Yu, X. Zhang, D. Wang, L. Wang, Y. Ma, Crystal Growth & Design 9 (2008) 528–533.
[28] S. Yoon, J.H. Jang, B.H. Ka, S.M. Oh, Electrochimica Acta 50 (2005) 2255–2262.
[29] J. Biener, M. Stadermann, M. Suss, M.A. Worsley, M.M. Biener, K.A. Rose, T.F. Baumann, Energy & Environmental Science 4 (2011) 656–667.
[30] R.K. Kalluri, M.M. Biener, M.E. Suss, M.D. Merrill, M. Stadermann, J.G. Santiago, T.F. Baumann, J. Biener, A. Striolo, Physical Chemistry Chemical Physics 15 (2013) 2309–2320.
[31] T.F. Baumann, M.A. Worsley, T.Y.J. Han, J.H. Satcher, Journal of Non-Crystalline Solids 354 (2008) 3513–3515.
[32] J. Chmiola, G. Yushin, Y. Gogotsi, C. Portet, P. Simon, P.L. Taberna, Science 313 (2006) 1760–1763.
[33] R.K. Kalluri, M.M. Biener, M.E. Suss, M.D. Merrill, M. Stadermann, J.G. Santiago, T.F. Baumann, J. Biener, A. Striolo, Physical Chemistry Chemical Physics 15 (2013) 2309–2320.
[34] R. de Levie, Advances in Electrochemistry and Electrochemical Engineering, vol. 6, Interscience Publishers, 1967.
[35] M.Z. Bazant, 10.626/10.426 Electrochemical Energy Systems, Massachusetts Institute of Technology, MIT OpenCourseWare, Spring 2011. http://ocw.mit.edu (accessed 24.03.13), License: Creative Commons BY-NC-SA.
[36] A. Mani, T.A. Zangle, J.G. Santiago, Langmuir 25 (2009) 3898–3908.
[37] T.A. Zangle, A. Mani, J.G. Santiago, Langmuir 25 (2009) 3909–3916.
[38] D.B. Robinson, Journal of Power Sources 195 (2010) 3748–3756.
[39] H. Marsh, F. Rodriguez-Reinoso, Activated Carbon, Elsevier Ltd., 2006.
[40] J. Segalini, B. Daffos, P.L. Taberna, Y. Gogotsi, P. Simon, Electrochimica Acta 55 (2010) 7489–7494.
[41] W. Sugimoto, H. Iwata, K. Yokoshima, Y. Murakami, Y. Takasu, Journal of Physical Chemistry B 109 (2005) 7330–7338.
[42] E. Frackowiak, F. Beguin, Carbon 39 (2001) 937–950.
[43] H. Gerischer, R. McIntyre, D. Scherson, W. Storck, Journal of Physical Chemistry 91 (1987) 1930–1935.